Laser and Particle Beams (2001), *19*, 267–284. Printed in the USA.

Implosion experiments of gas-filled plastic-shell targets with $\ell = 1$ drive nonuniformity at the Gekko-XII glass laser

MANABU HEYA, HIROYUKI SHIRAGA, ATSUSHI SUNAHARA, MIKIO NAKASUJI, MASAHARU NISHIKINO, HIROSHI HONDA, KAZUHISA FUJITA, NOBUHIKO IZUMI, NORIAKI MIYANAGA, HIROAKI NISHIMURA, HIROSHI AZECHI, SHUJI NARUO, HIDEAKI TAKABE, TATSUHIKO YAMANAKA, AND KUNIOKI MIMA

Institute of Laser Engineering, Osaka University, Suita, Osaka 565-0871, Japan

(RECEIVED 22 September 2000; ACCEPTED 9 December 2000)

Abstract

Effects of an implosion nonuniformity with $\ell = 1$ (ℓ: Legendre polynomial mode number) on the hot spark formation were investigated in a series of direct-drive implosion experiments at the Gekko-Xll glass laser (Yamanaka *et al.*, 1987). The implosion dynamics and the performance from the early to final stage of the implosion were observed with a variety of X-ray imaging and neutron diagnostics. A drive nonuniformity in the implosion with $\ell = 1$ was observed in the shape of the accelerated target at the early stage of the implosion. At the final stage of the implosion, the resultant nonuniformity with $\ell = 1$ was also observed as a geometrical shift of core plasmas from the center of the chamber. The observed neutron yield and X-ray emission properties at the final stage of the implosion were significantly degraded with an increase of the implosion nonuniformity with $\ell = 1$. The experimental results were compared with one-dimensional (1-D) and two-dimensional (2-D) hydrodynamic simulations. As a result, it was found that the implosion nonuniformity with $\ell = 1$ shifts the whole implosion dynamics towards its direction and prevents the confinement of the gas fuel considerably. However, the experimentally observed degradation in the hot spark formation, such as reductions in neutron yield and features in X-ray emission, can be reproduced in 2-D simulations not with an asymmetric perturbation of $\ell = 1$ only but with multimode nonuniformities such as $\ell = 1$ coupled with some additional middle-mode ones (e.g., $\ell = 6$). Such a complex spike structure caused by the multimode nonuniformities was found to be essential for the experimentally observed rapid cooling of the hot spark.

1. INTRODUCTION

In direct-drive laser fusion, a spherical shell target, which has an inner main fuel layer and an outer ablator layer and contains fuel gas inside, is imploded by high pressure induced by laser irradiation (Nuckolls *et al.*, 1972). The process of the implosion consists of two phases: (1) an acceleration phase in which the target is accelerated radially inward by the ablation pressure, and (2) a stagnation phase in which a hot spark ignitor with high temperature (>10 keV) and low density and the surrounding main fuel with low temperature and high density (500–1000 times liquid density) are formed. The kinetic energy of the accelerated shell must be efficiently converted to the thermal energy of the hot spark via PdV work in the stagnation phase. This scheme is called the "central ignition" scheme (Meyer-ter-vehn, 1982).

Current implosion experiments have been focused on a demonstration of this hot-spark/main-fuel structure in much smaller scales with currently available laser and target than the future ignition or high-gain conditions. High-density implosion of the main fuel has been successfully achieved already up to 600 times liquid density in experiments with hollow plastic (CD) targets. However, observed neutron yields in the experiments were much lower than those calculated with a one-dimensional (1-D) code, and it was concluded that the hot spark formation was significantly degraded in the stagnation phase due to implosion nonuniformities (Azechi *et al.*, 1991).

Hot-spark formation can be more clearly studied by using plastic-shell (CH) targets containing DD or DT gases as fuel gas inside. Such implosions can be considered as a model

Address correspondence and reprint request to: Manabu Heya, Institute of Free Electron Laser, Graduate School of Engineering, Osaka University, 2-9-5 Tsuda-Yamate, Hirakata, Osaka 573-0128, Japan. E-mail: heya@fel.eng.osaka-u.ac.jp

for creating the hot-spark/main-fuel structure, where the compressed DD or DT gases are regarded as the low-density hot spark and the surrounding plastic shell as the high-density main fuel. In many implosion experiments with spherical plastic or glass microballoon targets filled with DD or DT gases (Bayer *et al.*, 1984; Richardson *et al.*, 1986; Kilkenny *et al.*, 1988; Takabe *et al.*, 1988, 1989; Marshall *et al.*, 1989; Strom *et al.*, 1990; Andre *et al.*, 1992; Bradley *et al.*, 1992; Koenig *et al.*, 1992; Cable *et al.*, 1994; Dittrich *et al.*, 1994), the observed neutron yields were lower than the predicted values as described in Azechi *et al.* (1991), especially at implosions with high radial convergence ratios, where the ratio is defined as the initial radius of the fuel gas divided by the radius of the compressed one. These reductions in yield have been presumed to be caused by a fuel/shell mixing (Richardson *et al.*, 1986; Andre *et al.*, 1992; Dittrich *et al.*, 1994), by a three-dimensional (3-D) distortion of the core (Bayer *et al.*, 1984), and generally by a combination of those (Kilkenny *et al.*, 1988; Takabe *et al.*, 1988, 1989; Marshall *et al.*, 1989; Strom *et al.*, 1990; Bradley *et al.*, 1992; Cable *et al.*, 1994) in the stagnation phase. However, almost all of these analyses have been done by using data of core performances with time- and space-integrated neutron yield (except space-integrated neutron burn time (Kilkenny *et al.*, 1988; Cable *et al.*, 1994), time-integrated X-ray image (Richardson *et al.*, 1986), and time-resolved X-ray spectroscopic measurements (Dittrich *et al.*, 1994).

Factors that degrade the stable hot-spark formation can be classified into two groups: small-scale and long-scale perturbations. The small-scale perturbations, that is, high spatial mode nonuniformities, originating from the initial roughness of the target surface or from the imprinting of the irradiation nonuniformities (Desselberger *et al.*, 1992; Kalantar *et al.*, 1996; Azechi *et al.*, 1997) are amplified in the acceleration phase and then in the stagnation phase by Rayleigh–Taylor (RT) instability, which causes the mixing of the shell into the hot spark and degrades the hot-spark formation as observed in Dittrich *et al.* (1994). On the other hand, the long-scale perturbations, that is, low spatial mode nonuniformities, can also degrade the hot-spark formation via the distortion of the core, even if they would not be largely RT amplified because of the relatively low RT growth rate.

In this article, we focus on an $\ell = 1$ implosion nonuniformity, which is caused by a $\ell = 1$ drive nonuniformity whose level is changing shot by shot. The $\ell = 1$ nonuniformity shifts the whole core plasmas from the initial center of the target and noticeably prevents the compression of the gas fuel. From this point of view, we need to investigate how the $\ell = 1$ nonuniformity affects the hot-spark formation. In order to directly obtain information on the hot-spark formation, whose process is changing with time and space in the core and strongly affected by the implosion nonuniformity at the acceleration phase, it is of great importance to observe the dynamics not only at the stagnation phase but also at the acceleration phase with time- and space-resolved measurements.

We have performed a series of direct-drive implosion experiments in order to precisely understand how low-mode nonuniformities affect the hot-spark formation. Experimental conditions were carefully chosen to suppress the RT growth of high modes by introducing partially coherent light (PCL; Nakano *et al.*, 1993) and random phase plates (RPPs; Kato *et al.*, 1984) and by adding a prepulse to a drive laser pulse at the expense of higher adiabat (Kato *et al.*, 1996). In Section 2, the experimental conditions and the overall implosion dynamics from the acceleration to stagnation phase measured with a variety of X-ray imaging and neutron diagnostics including time- and space-resolved X-ray imagings are described. From the experimental results, we describe that shifts of the core plasmas from the initial center of the target are attributed to the implosion nonuniformity with $\ell = 1$ in the acceleration phase, and that core performances and X-ray emission features are degraded with an increase of the shifts of the core. In Section 3, the experimental results are compared with 1-D and 2-D simulations. Mechanisms of a degradation of the hot-spark formation due to low-mode nonuniformities are discussed. Section 4 is devoted to conclusions.

2. EXPERIMENTS AND RESULTS

We have carried out direct-drive implosion experiments with PCL output from the Gekko-XII glass laser facility (Yamanaka *et al.*, 1987). The PCL was introduced to reduce medium- to high-mode irradiation nonuniformities of more than $\ell = 20$ down to $\sigma_{\mathrm{rms}} = 1\%$ level or less at time-integration for 50–100 ps (Miyanaga *et al.*, 1996), where σ_{rms} is the irradiation nonuniformity evaluated as $\sigma_{\mathrm{rms}} = (\Sigma(\sigma_\ell)^2)^{1/2}$, and σ_ℓ is the nonuniformity of ℓth mode (Tsubakimoto *et al.*, 1998). The laser wavelength and total output energy were 0.527 μm and 3.0 kJ, respectively. The laser waveform was a 1.6-ns square pulse preceded by a 0.2-ns prepulse. The intensities of the prepulse and the square pulse were the same and the time gap between them was 0.4 ns. The typically measured power imbalance among the 12 beams was within $\pm 10\%$ in peak-to-valley. The laser beams were focused onto a spherical target with RPPs and F/3 lenses. The focusing condition d/R (where d is the distance between the center of the target and the focal point and R is the initial radius of the target) was set to be -3 or -4. The minus sign means that the focal point is beyond the center of the target.

Plastic shells used in this experiment were filled with fuel gas which is a mixture of hydrogen ($= 6$ atm) and deuterium ($= 4$ atm) gases with a small fraction of Ar ($= 0.025$ atm) and tritium ($= 0.02$ atm) gases as seed gas for X-ray and neutron diagnostics. The plastic shell was coated with 330-Å-thick Al to seal the fuel gas at room temperature. The decay constant of the fill pressure with the Al barrier layer was less than ~ 0.35 atm/h at the above condition and the

https://doi.org/10.1017/S0263034601192177 Published online by Cambridge University Press

tolerance of the fill pressure was up to ~9.6 atm (Takagi & Norimatsu, 1995). The diameter and thickness of the shell were 500 μm and 7 μm, respectively. Quality of the target was inspected so that the sphericity of the shell was better than 99% and the nonuniformity in shell thickness was less than 1%. The target was positioned to have its center on the center of the chamber within an accuracy of 10 μm.

When the target material is decompressed by the shock wave launched by the prepulse, the RT growth can be suppressed due to increased ablation velocity. The maximum e-folding ($\Gamma = \int \gamma dt$) of the RT growth was estimated to be $\Gamma = \sim 3.5$ for the mode number of $\ell \sim 50$ and $\Gamma \leqq \sim 2.5$ for $\ell \leqq 10$, when it is reduced by adding the prepulse (Kato *et al.*, 1996). Here, γ is the RT growth rate and t is time. The amplitude of the higher modes of $\ell > 20$ after the RT growth in the acceleration phase can be estimated as $A = A_0 \exp(\Gamma)$, where A_0 is an initial amplitude of the nonuniformity. The resultant amplitude for the initial roughness of the target was of the order of ~2.3 μm (= 0.01 (%) × 7 (μm) × exp(3.5)), while that for the imprinting of the irradiation nonuniformity ~1.7 μm (= 0.05 (μm) × exp(3.5)). Here, the initial amplitude of the irradiation nonuniformity was considered as an equivalent initial surface amplitude, which was experimentally observed in the similar laser conditions (Azechi *et al.*, 1997). Also, the calculated radial convergence ratio was ~13 at the maximum compression, resulting in the core radius ~20 μm (= 500/2/13). The amplitudes in both cases are negligibly small compared to the core radius. Therefore, we can presume that the hot-spark formation is not strongly affected by the higher-mode nonuniformities in this experiment.

A variety of X-ray imaging and neutron diagnostics were used to observe the overall implosion dynamics from the acceleration to stagnation phase from many directions as indicated with (θ, ϕ) coordinate in Figure 1. Details of each diagnostics are described later. We have focused on a dependence of the implosion nonuniformity with $\ell = 1$ on the hot-spark formation and have analyzed experimental results for typical two shots, a larger $\ell = 1$ implosion (Case A) and a smaller $\ell = 1$ implosion (Case B), comparing low-mode nonuniformities during the overall implosion and the core performance.

Figures 2(a) and 2(b) show time-integrated X-ray images of the core plasmas for Cases A and B, respectively. These images were obtained with three X-ray pinhole cameras (XPCs). Each XPC was equipped with an X-ray charged-coupled device (CCD) camera. The spatial resolution and observed X-ray spectral range of each XPC were 15 μm and roughly above 1.6 keV, respectively. Viewing directions of three XPCs were nearly orthogonal with each other. Observation angles of XPC-1, -2, and -3 in (θ (deg), ϕ (deg)) coordinate defined in Figure 1(a) were (45, 35.3), (45, −35.3), and (−45, −35.3), respectively. The central position of the chamber for each frame was determined within an accuracy of ±5 μm in a separate laser shot by using a thin cross wire target made of Au-coated C fibers with a diameter of 7 μm. One can see that the position of the observed core shifts from the center of the chamber, which indicates the existence of an implosion nonuniformity with mode number $\ell = 1$. The direction and distance of the shift can be derived from XPC's data in two directions with a 3-D stereo graphic analysis. The positions of the core shift shown in Figure 2(c) were derived from the data of XPC-1 and -2 for Cases A and B. The data of XPC-3 were not used because the calibration of XPC-3 had failed. In such a projection procedure, there is a possibility that a large error in core shift may be caused in the plane including XPC-1 and -2. Here, the core shift was defined as the distance between the center of the chamber and the center of the core defined as the position of the peak X-ray emission in the XPC's image. The positions and the distances for Cases A and B are (18 μm, 28 μm, 6 μm) and (4 μm, 12 μm, −5 μm) in (x, y, z) coordinate, and 34 ± 7 μm and 14 ± 6 μm, respectively. The errors correspond to inaccuracy of the position of the peak X-ray emission. From

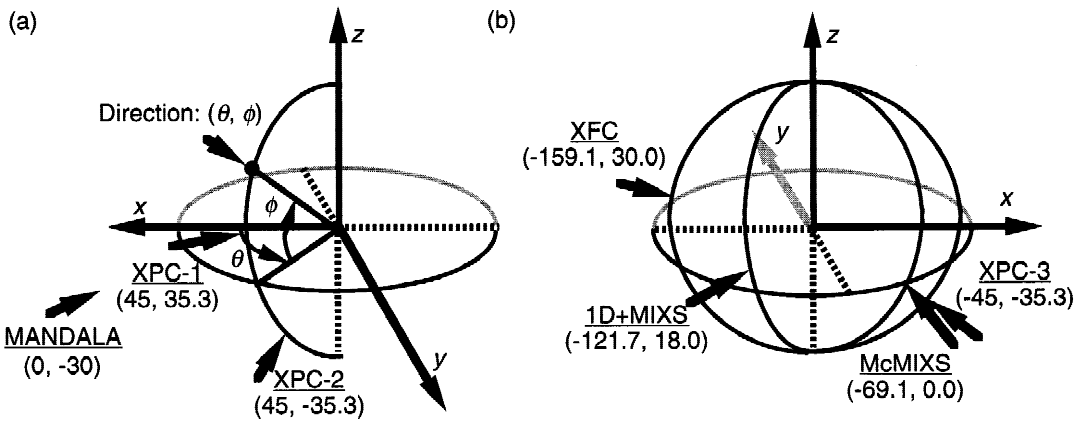

Fig. 1. Schematic figure of diagnostic setup viewing from one side (a), and from the opposite side (b). The observation angle of each diagnostics is shown in (θ (deg), ϕ (deg)) coordinate as defined in (a).

https://doi.org/10.1017/S0263034601192177 Published online by Cambridge University Press

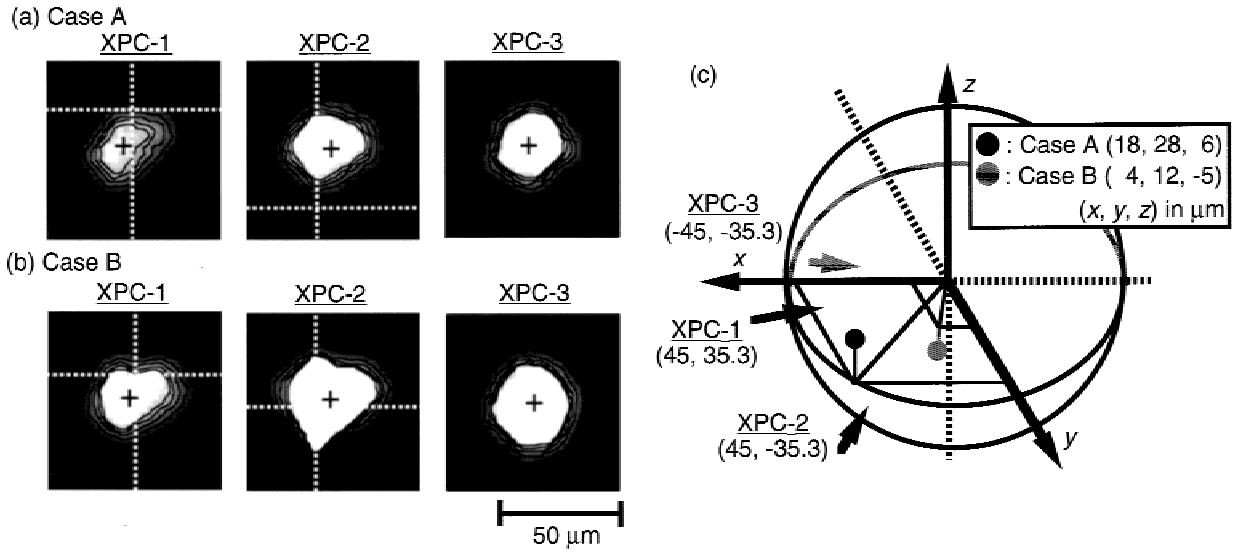

Fig. 2. Time-integrated X-ray images of the core for two shots of Cases A (a) and B (b) observed with the XPC-1, -2, and -3. Images were partially saturated. White dotted crosses and solid crosses show the central position of the chamber and the practical center of the core, respectively. The center of the chamber was not shown on the image of the XPC-3 because the calibration failed. (c) 3-D practical positions of the core for Cases A and B in (x, y, z) coordinate which is corresponding to (x, y, z) coordinates indicated in Figures 1 (a) and 1(b).

these results, it is found that the implosion nonuniformity with $\ell = 1$ is larger in Case A than in Case B and the direction of the core shift is different between the two cases.

In the following, we will compare the experimental results on (1) the shell motion in the acceleration phase and (2) the dynamics and performance of the core plasmas in the stagnation phase for Cases A and B.

2.1. Shell motion in acceleration phase

We used an X-ray framing camera (XFC) (Katayama *et al.*, 1991) to observe the implosion trajectory of the shell and its low-mode nonuniformities in the acceleration phase. The XFC had a temporal resolution of 80 ps, a spatial resolution of 18 μm, and a dynamic range of 130. The observed X-ray spectral range was determined by a combination of a 20-μm-thick Be filter and a Au photo-cathode to be about 1 keV and above.

Figure 3 shows raw data observed with the XFC for Case A implosion. The central position of the chamber for each frame was determined within an accuracy of ± 5 μm by using the same manner as the XPC and was defined as $(x_{\mathrm{XFC}}, y_{\mathrm{XFC}}) = (0,0)$. The difference in X-ray intensity between frames is mainly due to nonuniformity of the photocathode sensitivity, and does not exactly represent the difference in real X-ray intensity. From Figure 3, one can clearly see that the shell is being imploded with time, and the beginning of the X-ray emission from the core plasmas appears inside the imploding shell in frame 6. One can also see that the center of the imploding shell in frames 2–6 is gradually shifting towards the left-and-top direction from the center of the chamber in this view plane and the shape of the shell is close to but not a perfect circle and is being distorted with time.

For a comparison of the overall history of the experimentally observed implosion dynamics with a hydrodynamic simulation, we used a 1-D Lagrangian hydrodynamic code "ILESTA-1D" (Takabe *et al.*, 1988), which includes flux-limited two-temperature hydrodynamics, classical absorption of the incident laser calculated with ray tracing, and radiation transport with an averaged ion model for bound–free and free–free transitions.

Figure 4 shows a flow diagram calculated with the ILESTA-1D for Case A implosion. The average radius of the experimentally observed peak X-ray emission for each frame is shown in Figure 4 with an open circle. It was derived as the average distance between the position of the peak X-ray emission and the center of the chamber over an azimuthal angle of $\theta = 0$–$360°$ for each frame in Figure 3. On the other hand, the radius of the peak X-ray emission from the 1-D code is indicated in Figure 4 with a dotted line. It was calculated in the 1-D code taking into account emission and absorption of X rays along the line of sight. The spatial resolution and X-ray spectral response of the XFC were also taken into account in the calculation. The calculated and experimentally observed average radii of the peak X-ray emission are in good agreement. Thus, one may presume that the bulk motion of the shell is well described by the 1-D simulation, and the experimentally observed position of the peak X-ray emission from the shell represents the position of the ablation front. In the 1-D simulation, the positions of the peak X-ray emission, of the peak density, and of the peak

https://doi.org/10.1017/S0263034601192177 Published online by Cambridge University Press

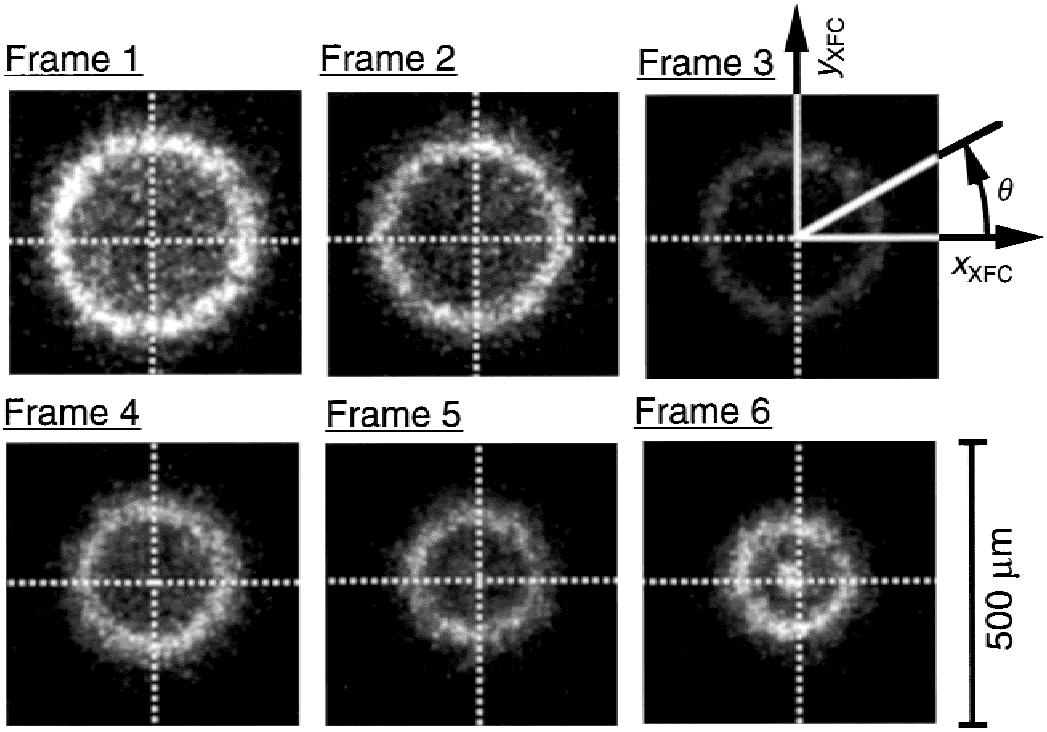

Fig. 3. Raw data observed with the XFC for Case A. The framing interval is 100 ps. θ denotes the azimuthal angle. A coordinate in this projected plane is indicated as (x_{XFC}, y_{XFC}) on frame 3. White dotted crosses show the center of the chamber.

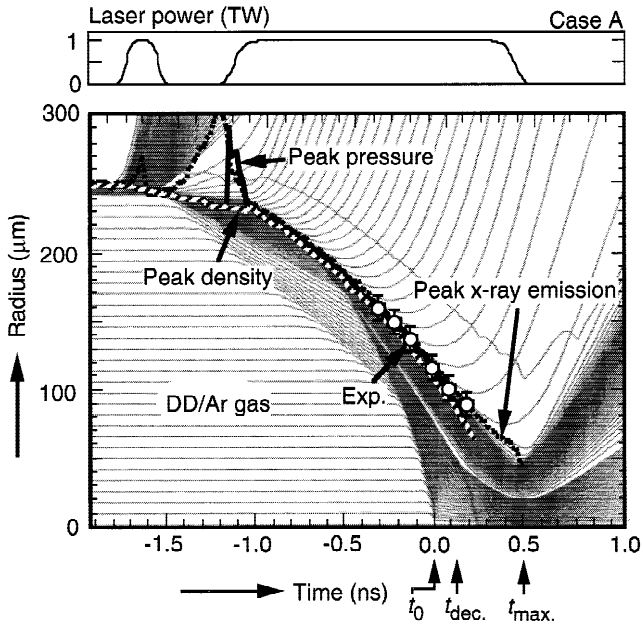

Fig. 4. Flow diagram calculated with the ILESTA-1D for Case A. Trajectories of the calculated peak X-ray emission, peak pressure, peak density, and the experimentally observed peak X-ray emission are plotted as functions of time. The time of t_0 ($t = 0$ ns), t_{dec}, and t_{max} represent the time of the first convergence of the shock at the center, the beginning of the deceleration of the shell, and the maximum compression in the 1-D simulation, respectively.

pressure are very close to that of the ablation front except the late frames 5 and 6. Then, the time-resolved 2-D structure observed with the XFC gives us information on 2-D distribution of the ablation front projected onto an observation plane, which is useful to estimate low-mode nonuniformities of the imploding shell in the acceleration phase.

Figure 5 shows results of modal analysis of the observed low-mode nonuniformities in the shape of the shell for Cases A and B. Figure 5(a) shows the radial position of the peak X-ray emission of the XFC's data for $\theta = 0$–$360°$ normalized to the initial radius of the target. It is clearly seen that the uniformity of the normalized radius for $\theta = 0$–$360°$ is better in Case B than in Case A. Assuming that an implosion velocity is constant in time during a period covered by the XFC's data, the implosion velocity can be derived from a linear fitting of the data of Figure 5(a). Figure 5(b) shows distributions of the implosion velocity as a function of θ for Cases A and B. The radial position of the shell at the time of t_0, defined as the time of the first shock convergence as indicated in Figure 4, can be derived from the data of the position and velocity by a linear interpolation. Resultant modal analyses of the position perturbation at $t = t_0$ and of the velocity perturbation are shown in Figures 5(c) and 5(d), respectively. Note that the calculated mode number is not one of the spherical Legendre polynomials but of a circular mode on the projected viewing plane of the XFC.

https://doi.org/10.1017/S0263034601192177 Published online by Cambridge University Press

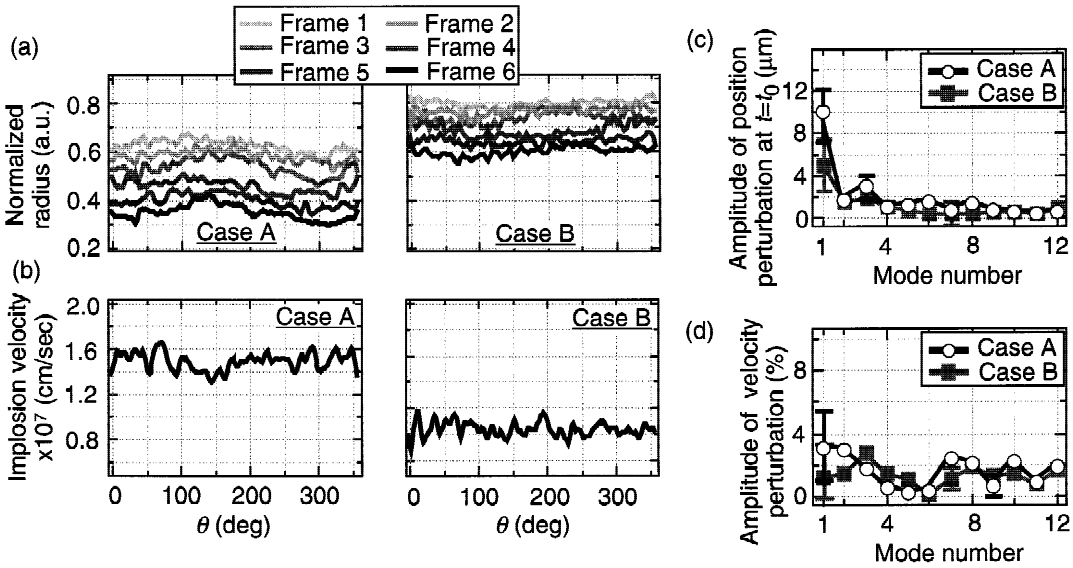

Fig. 5. Modal analyses on the observed low-mode nonuniformities of the shape of the shell for Cases A and B. (a) Normalized radial positions of the peak X-ray emission for each frame as functions of θ. (b) Distributions of the implosion velocity as a function of θ. (c) Modal amplitudes of the position perturbations in the viewing plane extrapolated to the time of t_0. (d) Modal amplitudes of the velocity perturbations.

The indicated error bars are due to uncertainty of the center determination including noises from the image recording system. Errors due to the temporal resolution of the XFC including a finite propagation speed of a voltage pulse were estimated and were negligible.

Low-mode nonuniformities with $\ell \leqq \sim 12$ are obvious in Figures 5(c) and 5(d). Higher modes with $\ell \geqq \sim 15$ are not observable due to spatial resolution limit of the XFC. A trend is seen that the radius is large at $\theta = 130$–$170°$ and 180–220° for Cases A and B, respectively, indicating the existence of the implosion nonuniformity with $\ell = 1$. Its displacement is larger in Case A (10 μm) than in Case B (5 μm), and the $\ell = 1$ velocity perturbation is $3.1 \pm 2.5\%$ for Case A and $1.2 \pm 2.5\%$ for Case B in the plane observed with the XFC.

The direction and amplitude of the $\ell = 1$ nonuniformity observed with the XFC are consistent with the position of the core shift observed with the XPC as described below. The position of the core observed with the XPC in (x, y, z) coordinate can be projected by calculation on the 2-D viewing plane of the XFC as $(x_{\mathrm{XFC}}, y_{\mathrm{XFC}})_{\mathrm{XFC}} = (20\ \mu\mathrm{m}, 19\ \mu\mathrm{m})_{\mathrm{XFC}}$ and $(-10\ \mu\mathrm{m}, 0.5\ \mu\mathrm{m})_{\mathrm{XFC}}$ for Cases A and B, respectively. The expected shift is $(20^2 + 19^2)^{1/2} = 28\ \mu$m and $(10^2 + 0.5^2)^{1/2} = 10\ \mu$m in a direction of $\theta = 133°$ and 183° for Cases A and B, respectively. The projected values of the core shift from the XPC's data are larger by a factor of about two than the amplitudes of the $\ell = 1$ nonuniformity observed with the XFC as shown in Figure 5(c), because the XPC's data are for the final core while the XFC's data extrapolated to $t = t_0$ are for the imploding shell with a radius of about half of the initial radius as shown in Figure 4. Therefore, the XFC's data are roughly in agreement with the XPC's one as described above, and the observed shift of the core can be concluded to have resulted from the $\ell = 1$ nonuniformity in the accelerating shell.

A clear difference between the two cases in amplitude and direction of the $\ell = 1$ nonuniformity was recognized. Also, it was seen from Figures 5(c) and 5(d) that there are other low-mode nonuniformities with $\ell = 2$–12, although their amplitudes are relatively small.

The observed implosion nonuniformity with $\ell = 1$ can be caused by a $\ell = 1$ perturbation in the irradiation nonuniformity of the drive laser and/or the target structural nonuniformity. In separate experiments (Heya *et al.*, 2000) at similar target and laser conditions, it was found that the observed nonuniform shape of the accelerated shell is strongly dependent on the observed distribution of the absorbed laser intensity. Hence, in the present experiments, the observed implosion nonuniformity with $\ell = 1$ in the accelerating shell results from the $\ell = 1$ drive nonuniformity. Note that the $\ell = 1$ perturbation in the implosion velocity is not amplified by RT growth, but results simply from the nonuniform acceleration because the e-folding of the RT growth for such a long wavelength perturbation is $\Gamma \leqq \sim 2.5$ and is small enough. There are many possible origins to cause the $\ell = 1$ drive nonuniformity such as power imbalance among 12 laser beams, initial displacement of the target from the center of the chamber due to inaccurate positioning, error in pointing of the focused laser beam, and distortion in the focused beam pattern. We do not have further information that would enable us to determine which are dominant in the present experiments.

https://doi.org/10.1017/S0263034601192177 Published online by Cambridge University Press

2.2. Dynamics and performance of core plasmas in stagnation phase

The formation process of the hot spark was investigated by observing X rays and neutrons emitted from the compressed fuel gas. We used time- and space-resolved X-ray imagings including a 1D+MIXS system and a McMIXS system, and a neutron spectrometer system (MANDALA).

A combination of one-dimensionally space-resolved and multi-imaging X-ray streak camera (MIXS) techniques (Shiraga *et al.*, 1997), 1D+MIXS method, was used to measure the implosion dynamics of the shell together with the core dynamics. The 1D+MIXS system provides 1-D spatial distribution at the equator of the imploding shell with a conventional use of an X-ray streak camera (XSC) and time-resolved 2-D images of the core plasmas with a MIXS method (Shiraga *et al.*, 1995). A principle of the 1D+MIXS is shown in Figure 6. Images of a source were made by doubly arrayed pinholes on a double slit photocathode of the XSC. Pinholes were made on a 25-μm-thick Ta disk. The pinhole disk was located 143 mm from the target and was covered with a blast shield plate (BSP) made of a 25-μm-thick Be disk. The distance from the pinhole disk to the photocathode was 1115 mm. The magnification was 1115/143 = 7.8. X-ray filters were placed in front of the pinhole disk. The photocathode with slits A and B in parallel was a 0.11-μm-thick CuI on a substrate made of a 0.1-μm-thick Parylene (C_8H_8). Each cathode slit size was 80 μm in width and 25 mm in length. The images on the cathode slits were streaked with the XSC (Hamamatsu C-2590), and were recorded with a 512 $\times$ 480-pixel cooled CCD camera (Hamamatsu C-3140).

Conventional 1-D space-resolved images A1–A3 at the equator of the imploding target were made on the photocathode slit A with the corresponding three pinholes, which were aligned on a straight line parallel to the cathode slit. The separation distance between pinholes was 350 μm. Different X-ray spectral responses and pinhole sizes for images A1–A3 were set to cover wide ranges of X-ray emissions from the imploding shell and the core plasmas. Diameters of the pinholes A1, A2, and A3 were 16.5 μm, 17.0 μm, and 29.0 μm, respectively. X-ray filters for images A1, A2, and A3 were a 500-μm-thick Be, a 35-μm-thick CHCl, and nothing, respectively. Observed X-ray spectral responses for filter/photocathode combinations used in this experiment are shown in Figure 7.

An array of 11 pinholes tilted with an angle of θ_{tilt} from the horizontal cathode slit was used to observe information at different positions of the source with the MIXS method. The separation distance between each pinhole was 150 μm. Eleven images, B1, B2,…, and B11, were made on the cathode slit B as shown in Figure 6(a). The images at different positions of the source were selected by the cathode slit with a constant vertical sampling distance as a set of divided 1-D images. The images were streaked with the XSC and were sliced at a given time. The time-sliced, divided 1-D image cells were rearranged from left to right to top to bottom. And then, the time-resolved, 2-D configuration of the original source was obtained. The X-ray filter used was a 35-μm-thick CHCl, which was the same as channel A2.

The spatial resolutions for channels A1, A2, and A3 were 25 μm, 25 μm, and 37 μm, respectively. The spatial resolution for channel B (MIXS) was 15 μm. The temporal resolutions for cathode slits A and B were 29 ps.

Raw data for Case B are shown in Figure 6(b). The X-ray emission in image A3 with a spectral response in relatively low photon energy is considered to be mainly from the outer shell, while those for A1, A2, and B1–B11 in relatively high energy photons are from the Ar ions in the core plasmas. This was confirmed in a separate shot with no Ar dopant by observing much weaker X-ray emissions in channels A1, A2, and B1–B11. MIXS images B1–B11 have a low signal level because of the poor sensitivity of the photocathode. Relative time between the implosion trajectory recorded in images A1–A3 and the core dynamics observed in the MIXS (B1–B11) images can be precisely determined from the vertical distance between slits A and B. Thus, the experimen-

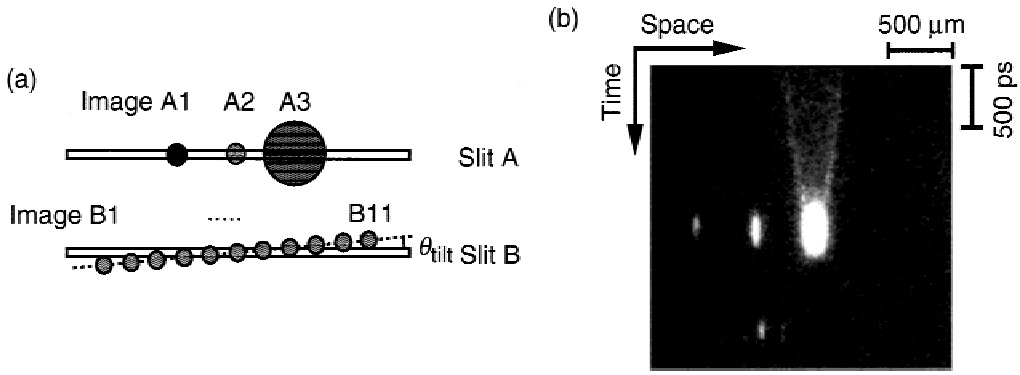

Fig. 6. Principle of the 1D+MIXS imaging. (a) Images A1–A3 are aligned on the cathode slit A. Images B1–B11 are aligned on the cathode slit B with a tilting angle. (b) Raw data observed with the 1D+MIXS system for Case B implosion.

https://doi.org/10.1017/S0263034601192177 Published online by Cambridge University Press

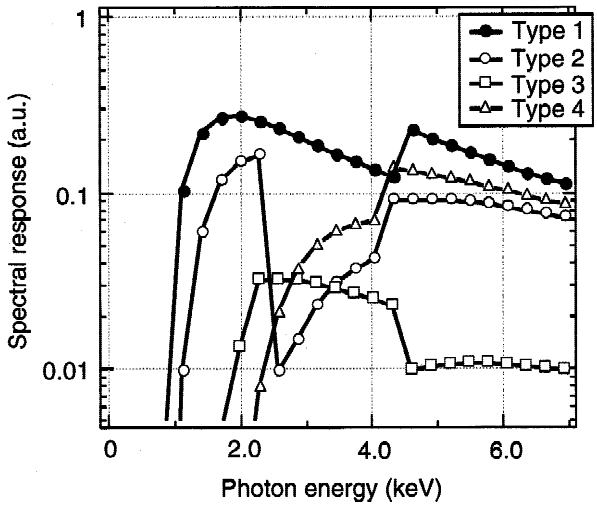

1D+MIXS	McMIXS
Channel A1: Type 4	Ch. A: Type 2
Channel A2: Type 2	Ch. B: Type 3
Channel A3: Type 1	Ch. C: Type 4
Channel B (MIXS): Type 2	

Fig. 7. X-ray spectral responses for filter/photocathode combinations used in this experiment. Combinations of filter/photocathode for types 1–4 are the BSP/CuI, a 35-μm-thick CHCl plus the BSP/CuI, a 3-μm-thick Ti plus the BSP/Au, and a 500-μm-thick Be plus the BSP/CuI, respectively. Types 1–4 are indicated with closed circles, open circles, open squares, and open triangles, respectively.

tally observed temporal behavior of the core plasmas in an absolute time scale can be compared with the 1-D simulation within an accuracy better than 30 ps by adjusting the experimentally observed trajectory of the shell implosion to that of the 1-D simulation.

Figure 8 shows streaked images A2 and A3 for Cases A and B in the stagnation phase. It is seen that (1) the shell starts to shift towards left at $t = 0.30$ ns (t_{shift}) in image A3 for Case A, which probably results from the nonuniform implosion with $\ell = 1$; (2) the X-ray intensity from the core plasmas starts to decrease at $t = t_{\text{shift}}$ in image A2 for Case A; (3) both the shift of the shell and the decrease in X-ray intensity from the core since $t = 0.30$ ns are not obvious for Case B; (4) the intensity and duration of the X-ray emission for Case B are higher and longer than those for Case A. These results show that the hot-spark formation for Case B with a less $\ell = 1$ nonuniformity was performed more stably than that for Case A. The positions of the core shift in a horizontal direction in images A2 and A3 are below 10 μm and less than the spatial resolution, and are also in good agreement with the projected XPC's core positions.

A multichannel, multi-imaging X-ray streak camera (McMIXS) method (Heya *et al.*, 1997), which provides multichannel 2-D images of the source with a high temporal

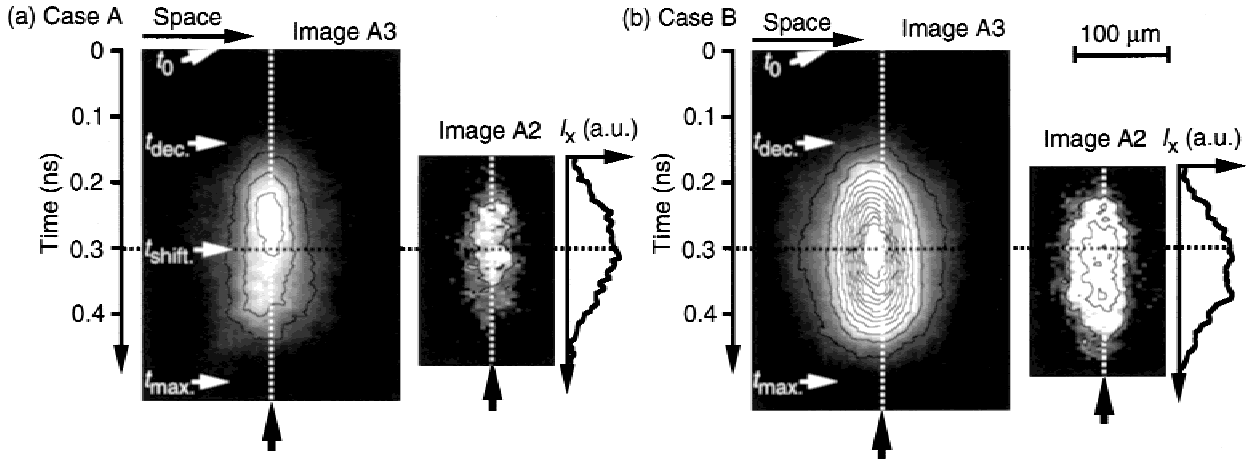

Fig. 8. Streaked images of channel A2 (the core) and A3 (the shell around the core) in the stagnation phase. Space-integrated temporal profiles of image A2 are also shown. The relative time is corresponding to the time indicated in Figure 4. The time of 0 ns corresponds to the time of t_0 in the 1-D simulation. The times of t_{dec} and t_{max} as defined in Figure 4 are also indicated. White dotted lines represent the center of the chamber. Contours for images A2 and A3 are shown at an interval of 60 and 200 counts in X-ray intensity (a.u.), respectively. The projected XPC's core positions in a horizontal direction are also shown with bold arrows.

https://doi.org/10.1017/S0263034601192177 Published online by Cambridge University Press

resolution, was used to obtain three-channel, 2-D X-ray images of the core plasmas in various spectral ranges. A schematic figure of the system is shown in Figure 9(a). A pinhole camera with three pinhole arrays was used to form three image arrays of the source on the corresponding three cathode slits of the streak camera. Each image array was tilted from the cathode slit with a slight angle. Three different filter/photocathode combinations were coupled to each image array. Applying the MIXS procedure, one can get time-resolved, three-channel, 2-D configurations of the original source [Figs. 9(b)–9(d)].

Specifications of the pinhole camera and the streak camera used in the McMIXS system are as follows. The distances from the center of the chamber to the pinhole disk and from the pinhole disk to the photocathode were $g = 84$ mm and $f = 1323.4$ mm, respectively, resulting in the image magnification $M = f/g = 15.8$. The pinhole disk with three arrays of 11 pinholes per array was made of a Ta disk with a thickness of 25 μm. A diameter of each pinhole was 11.5 μm within a variation of $\pm 5\%$. The horizontal distance between each pinhole and the vertical distance between each image array were $s = 100$ μm and $L_{\mathrm{PH}} = 208$ μm, respectively. A 25-μm-thick Be disk was placed in front of the pinhole disk as the BSP. We made three broadband X-ray spectral responses. The filter/photocathode combinations used were a 35-μm-thick CHCl/CuI (Ch. A), a 3-μm-thick Ti/Au (Ch. B), and a 500-μm-thick Be/CuI (Ch. C), respectively. Ch. A, B, and C had the sensitivity in the range of 1.0 keV and above, 2.2–4.9 keV, and 2.5 keV and above, respectively, as shown in Figure 7. Here, Ch. A was set to have the same spectral response as channel MIXS (B) of the 1D+MIXS to compare them directly. The XSC, CCD camera, and image analyzer used were similar types as with the 1D+MIXS.

The spatial and temporal resolutions of the McMIXS were 15 μm and 23 ps, respectively. The relative time between the 1-D simulations and the experiments was determined within an error of ± 30 ps by fitting temporal properties of the X-ray emission between Ch. A of the McMIXS and channel MIXS (B) of the 1D+MIXS.

Figure 10 shows experimental results observed with the McMIXS. Figures 10(a) and 10(b) show reconstructed 2-D X-ray images of the core plasmas for Cases A and B obtained with Ch. B of the McMIXS. The position of the core shifts more in Case A than in Case B. Here, we defined the practical center of the core as the position of the peak X-ray intensity in the time-integrated 2-D X-ray image obtained by accumulating McMIXS frames. The projected position of the core shift from observation with the XPC to the McMIXS's viewing plane is not in good agreement with the core observed with the McMIXS. As described before, this noticeable difference between them is probably due to a large error in the projection procedure when the observation angle of the McMIXS is almost orthogonal with those of XPC-1 and -2. Figure 10(c) shows temporal profiles of the experimentally observed X-ray intensity at the practical center of the compressed core for Cases A and B, and that calculated with the 1-D code for Case A. One can directly compare the experimentally observed temporal profiles for Cases A and B with the 1-D simulations in the following manner. In the 1-D simulation for a perfectly spherical im-

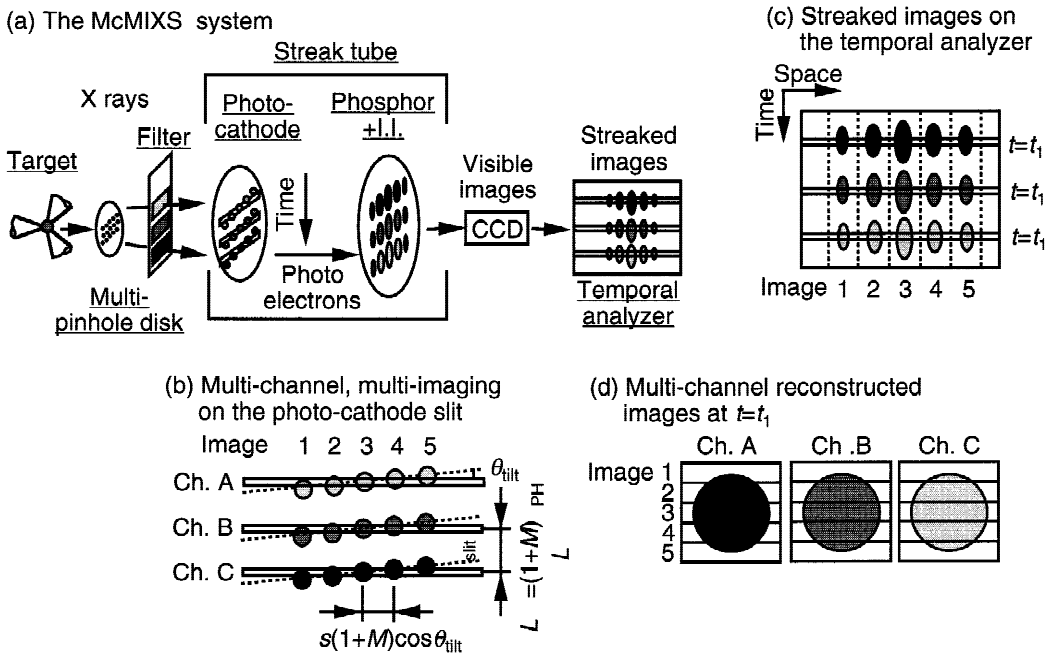

Fig. 9. Principle of the McMIXS system and 2-D image reconstruction. The number of images N is 5 in this example. M, s, L_{PH}, and L_{slit} are the magnification of the pinhole camera, the horizontal distance between each pinhole, the vertical distance between each image array, and the vertical distance between each cathode slit, respectively.

https://doi.org/10.1017/S0263034601192177 Published online by Cambridge University Press

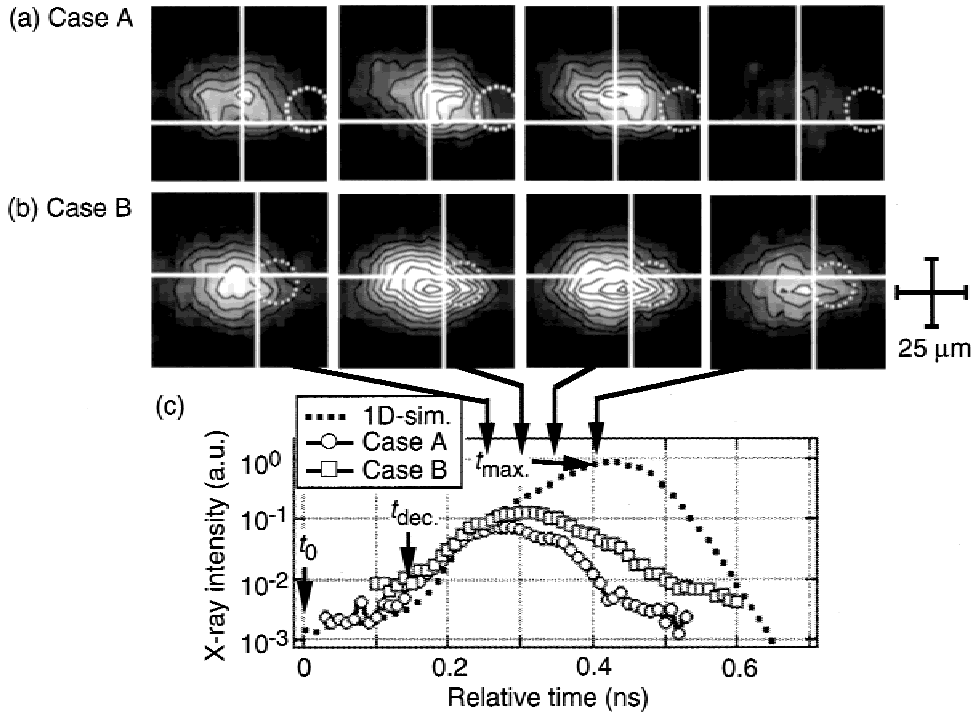

Fig. 10. Experimental results observed with the McMIXS for Cases A and B. Time-resolved 2-D X-ray images of the core plasmas for Cases A and B are shown in (a) and (b), respectively. White crosses and solid crosses indicate the center of the chamber and the practical center of the core, respectively. The projected XPC's core positions are also indicated with large dotted circles within an accuracy of ± 15 μm. The contour is shown at an interval of 192 counts in X-ray intensity (a.u.). (c) Temporal profiles of the X-ray intensity at the practical center of the core. The relative time is indicated according to the 1-D simulation in Figure 4. The times of t_0, t_{dec}, and t_{max} as defined in Figure 4 are also indicated.

plosion, the calculated implosion dynamics for Case B showed a small change from Case A since implosion conditions, such as laser energy and target size, for Cases A and B were slightly different by a few percent. For example, the calculated implosion time (t_{max}) was about 0.10 ns earlier in Case A than in Case B, and the calculated peak X-ray intensity at the central position of the core was 1.34 (K_{amp}) times larger in Case A than in Case B. However, the calculated temporal profiles of the X-ray intensities from $t = t_0$ for each case were seen to be similar within an accuracy of a few percent if those are normalized to the corresponding peak values for Cases A and B. Therefore, the calculated temporal profile for Case A shown as 1D-sim. in Figure 10(c) can be regarded as a standard profile for the perfectly spherical implosion for the both cases. To directly compare the experimental results with the simulations in temporal behavior, the experimentally observed temporal profile of Case A and K_{amp} times multiplied profile of Case B were fitted to this standard 1D-sim. profile with the same fitting coefficient at the early rising part of the X-ray emission (t = 0.15–0.25 ns). Here, we assumed that the experiments were in agreement with the 1-D simulation at this period.

From Figure 10, it is seen that (1) the observed X-ray images for both Cases A and B have low-mode nonuniform structures, which are changing with time, and the X-ray emission disappears earlier in Case A by about 0.10 ns than in Case B, which is consistent with the results in Figure 8; (2) the shape of the X-ray emission is more uniform in Case B than in Case A; (3) the position of the peak X-ray emission does not move much during the lifetime of the core; (4) the observed temporal properties of the X-ray emission show a good agreement with that calculated with the 1-D code only until t = 0.25 ns, which is about 0.12 ns after $t = t_{dec}$, the beginning of the deceleration of the shell, while a clear difference among Cases A, B, and the 1-D simulation is seen in the late period ($t > 0.30$ ns). These results indicate that there is a clear difference between Cases A and B in core performance at the late period in the stagnation phase, which is consistent with the data observed with the XPC, XFC, and 1D+MIXS.

A 960-channel efficient neutron time-of-flight (TOF) spectrometer system (MANDALA) (Izumi *et al.*, 1999) was used to measure neutron spectra, which provide information on neutron yield and ion temperature of the compressed fuel. The ion temperature (T_i) can be deduced from a primary DD neutron energy spread (Brysk, 1973). In Figure 11, neutron yield ratios of the observed DD neutron yields to those from the corresponding 1-D simulations and the observed ion temperature are plotted as functions of the position of the core shift observed with the XPC. The ob-

https://doi.org/10.1017/S0263034601192177 Published online by Cambridge University Press

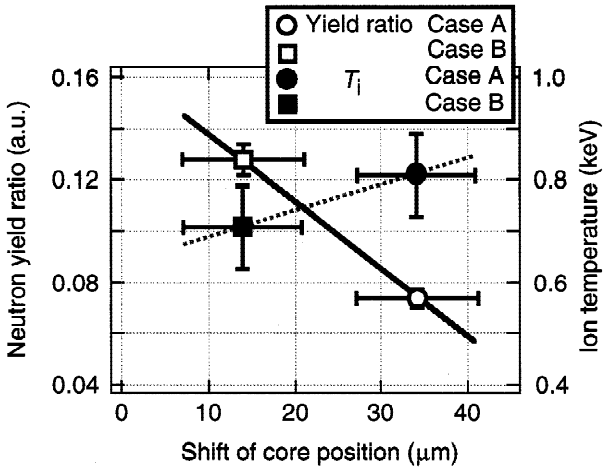

Fig. 11. Dependence of the experimentally observed neutron yield and the ion temperature on the shift of the core position.

served neutron yield ratio decreases with an increase of the core shift. On the other hand, the ion temperature is almost constant within the error bars.

The summary of the experimental results from the acceleration to stagnation phase for Cases A and B is as follows: (1) The $\ell = 1$ nonuniformity was observed in the implosion dynamics of the accelerating shell, and it was larger in Case A than in Case B. The existence of other low-mode (ℓ = 2–12) nonuniformities was also recognized. (2) The position of the core shifted from the center of the chamber. The direction and amplitude of the core shift were consistent with the $\ell = 1$ nonuniformity in the imploding shell. (3) The position, shape, and performance of the core showed better features in Case B than in Case A.

Thus, the implosion nonuniformity with $\ell = 1$ was clearly observed from the acceleration to stagnation phase. The $\ell = 1$ nonuniformity prevents the confinement of the fuel gas in the stagnation phase, resulting in the degradation of the hot-spark formation. As described before, sources of the observed implosion nonuniformity with $\ell = 1$ cannot be determined in the present experiments. However, we can focus on the implosion dynamics and core performance with $\ell = 1$ in order to precisely understand the observed rapid cooling of the hot spark in the stagnation phase. Also, we consider the other observed low-mode nonuniformities such as $\ell = 6$, which will be described in Section 3. We presume that the difference in uniformity of the accelerating shell leads to the difference in hot-spark formation in the stagnation phase, and will examine that by comparing the experimental results, such as neutron and X-ray data, with 2-D simulations in Section 3.

3. DISCUSSION

To qualitatively and quantitatively understand effects of low-mode nonuniformities in implosion on its core performance and dynamics, we have carried out 2-D simulations and compared the results with the experimentally observed neutron and X-ray data.

An axisymmetrical 2-D Eulerian Godunov code with Spitzer–Härm electron thermal conduction for an ideal plasma was used (Sunahara & Takabe, 1996). In the 2-D calculation, ion and electron temperatures were assumed to be the same because a temperature relaxation time is of the order of a few picoseconds and short enough compared to a typical time scale of the dynamics in the stagnation phase. Radiation transport was calculated based on a flux-limited diffusion approximation model. An X-ray spectrum from the core plasmas, which corresponds to the experimental results for Ch. B of the McMIXS, was calculated by using emissivity and opacity tables obtained with an averaged ion model.

For simplicity of the 2-D calculation, the implosion dynamics until $t = t_0$, which corresponds to the time when the converging shock wave collides at the center of the target, was assumed to be a perfectly spherical implosion and was calculated by using the 1-D spherical code, ILESTA-1D. And then, physical parameters obtained with the 1-D code were transferred to the 2-D code with an assumption that the target keeps a spherically symmetric shape at $t = t_0$. The 2-D code was used to calculate the implosion dynamics after $t = t_0$. Low-mode perturbations only in implosion velocity were introduced to a spherical core plasma as an initial condition at $t = t_0$ in the 2-D calculation. This assumption may be adequate for $\ell = 1$ as a rough approximation. If the implosion has the $\ell = 1$ velocity perturbation until $t = t_0$, it would cause a shift of the position of the core from the initial center. However, its shape for $\ell = 1$ may still remain nearly spherical at $t = t_0$. Thus, the center in the 2-D code should not be regarded as the position of the initial center but as the center of the shifting core. On the other hand, this assumption is obviously not realistic for perturbations with higher modes, $\ell \geqq 2$, which result in the distorted core shape even at $t = t_0$.

We focus our interest on the large nonuniformity with $\ell = 1$ (asymmetric perturbation) observed in the experiments, and consider the other observed low-mode (ℓ = 2–12) ones with smaller amplitudes by representing them with a $\ell = 6$ (symmetric and middle-mode perturbation) as an additional effect to $\ell = 1$. The implosion nonuniformity with $\ell = 6$ was chosen because it is known as a typical nonuniform mode caused by a dodecahedral geometry of the Gekko-Xll laser facility (Miyanaga *et al.*, 1996). Note that implosion nonuniformities close to $\ell = 6$ are assumed to make little difference with $\ell = 6$ from a point of view on a symmetric perturbation. Two-dimensional simulations were carried out to find conditions for reproducing the experimental results with a single mode ($\ell = 1$ or $\ell = 6$) nonuniformity, or multimode ($\ell = 1$ and $\ell = 6$) ones. The amplitudes of the velocity perturbations with mode numbers 1 (NU_1) and 6 (NU_6) were varied in ranges of NU_1 = 0–27% and NU_6 = 0–20%, respectively. The direction of NU_1 was set from the bottom to the top in the 2-D calculation plane, and that of NU_6 was set to be axisymmetrical around the NU_1 axis.

https://doi.org/10.1017/S0263034601192177 Published online by Cambridge University Press

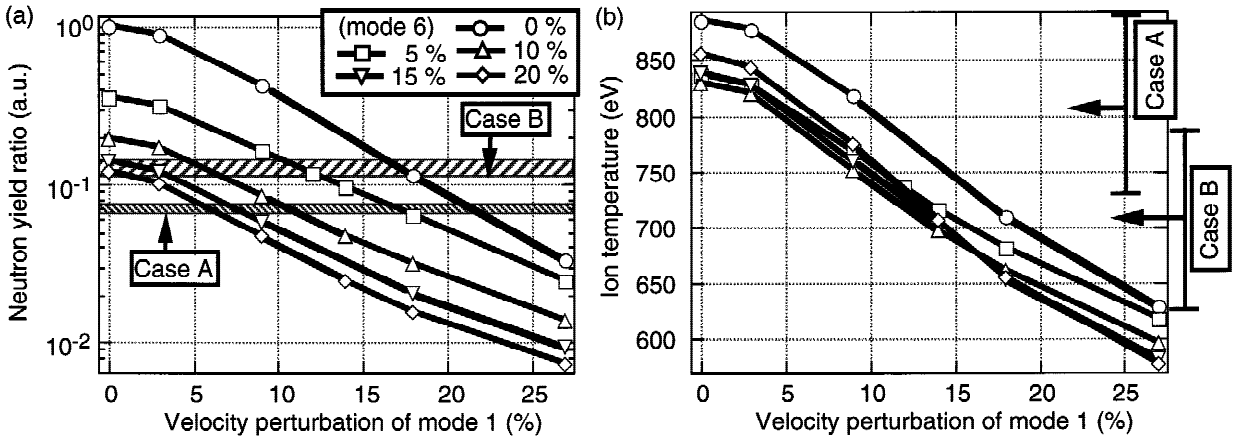

Fig. 12. Dependence of the (a) neutron yield and (b) ion temperature on NU_1 and/or NU_6 by 2-D simulations. Experimental results for Cases A and B are also indicated.

Neutron yield dependence on NU_1 and/or NU_6 by 2-D simulations is shown in Figure 12(a). Neutron yields from the 2-D simulations were normalized to that calculated for a perfectly spherical implosion with $NU_1 = NU_6 = 0$. The experimentally observed neutron yields normalized in the same manner are also plotted for Cases A and B. The calculated neutron yields have a general tendency to decrease with an increase of nonuniformities for both NU_1 and NU_6. When only NU_1 is varied and $NU_6 = 0$, the calculated yield decreases monotonically with an increase of NU_1. If the

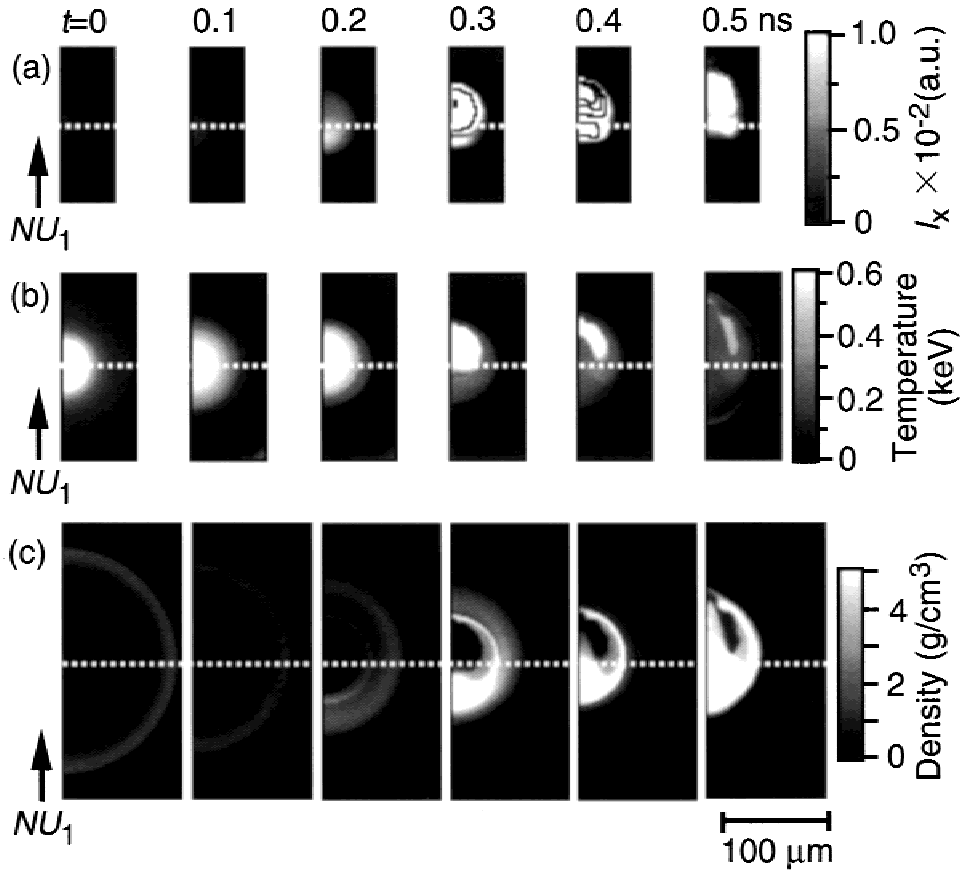

Fig. 13. Calculated snapshots of (a) 2-D X-ray projection images, and (b) temperature and (c) density distributions at the cross section of the target including the center for the implosion with $\ell = 1$ nonuniformity ($NU_1 = 18\%$, $NU_6 = 0$). The contour for the 2-D X-ray image is shown at an interval of 0.04 in X-ray intensity (a.u.).

https://doi.org/10.1017/S0263034601192177 Published online by Cambridge University Press

difference in observed neutron yield for Cases A and B is attributed to NU_1 only, the required increase in NU_1 from Case B to Case A is from $NU_1 = 17\%$ to 22%. When NU_6 is added to NU_1, the calculated yield decreases with an increase of NU_6 for all NU_1 cases examined here. The required increase in NU_1 from Case B to Case A is, for example, 12% to 17% at $NU_6 = 5\%$, 6% to 10% at $NU_6 = 10\%$, and 3% to 7% at $NU_6 = 15$–20%, respectively. The relative phase between NU_1 and NU_6 is another parameter in the 2-D simulation, and we verified that the 2-D simulation results show a similar tendency of the yield reduction in many cases with various phase differences. Thus, the observed neutron yields for Cases A and B can be explained in these ranges of NU_1 and NU_6 values. However, it was found impossible to reproduce the yield reduction in Case A if only NU_6 is considered and $NU_1 = 0$. To explain the observed neutron yield for Case A in 2-D simulations with only NU_6, it is necessary to increase NU_6 to an unrealistic higher value more than 30–40%. This value gives us the distortion of the shell with an amplitude of $\sim$100 μm and is too large to explain the observed X-ray data with 2-D simulations (see Figs. 18 and 19).

Figure 12(b) shows ion temperature dependence on NU_1 and/or NU_6 by 2-D simulations. The experimental results are also indicated for Case A and Case B. The calculated ion temperature was weighted by the neutron emission rate, which corresponds to that observed with the TOF spectrum. The 2-D simulation shows the reduction in ion temperature only by about 50 eV for NU_6 up to 20%, and a gradually decreasing feature by about 200 eV for NU_1 up to 20%. It is seen that the calculated ion temperature in these parameter ranges is in agreement with the experimental results within the error bars.

Temporal behaviors of the core plasmas observed in the time-resolved 2-D X-ray images were compared with 2-D simulation results considering the effects of NU_1 and/or NU_6. First, Figure 13 shows calculated snapshots of (a) 2-D X-ray projection images, and (b) temperature and (c) density distributions at the cross section of the target including the center for the implosion when only the $\ell = 1$ nonuniformity is introduced ($NU_1 = 18\%$, $NU_6 = 0$). Only the right half plane of the target is shown in Figure 13. The relative time $t = 0$ (t_0) corresponds to the time when the converging shock wave collides at the center of the target as previously defined in Figure 4. The velocity perturbation NU_1 was set to have the maximum velocity at the bottom of the target and the minimum at the top. White dotted lines indicate the horizontal axis.

Figure 13(c) shows that a spike comes up from the shell at the bottom into the inner fuel gas region and penetrates upward through it. As shown in Figure 13(b), the temperature is relatively low in the spike structure, and the fuel region is cooled down by the intrusion of the cold spike. Figure 13(a) shows calculated 2-D X-ray images. X rays are mainly emitted from Ar ions doped in the fuel. X-ray images are seen to be corresponding roughly to the temperature distributions in Figure 13 (b). It is also seen that the region of the calculated intense X-ray emission is in the lower part of the fuel at $t =$ 0.2 ns, and moves about 50 μm upward as the spike intrudes and cools down the fuel during $t = 0.2$–0.5 ns. This feature

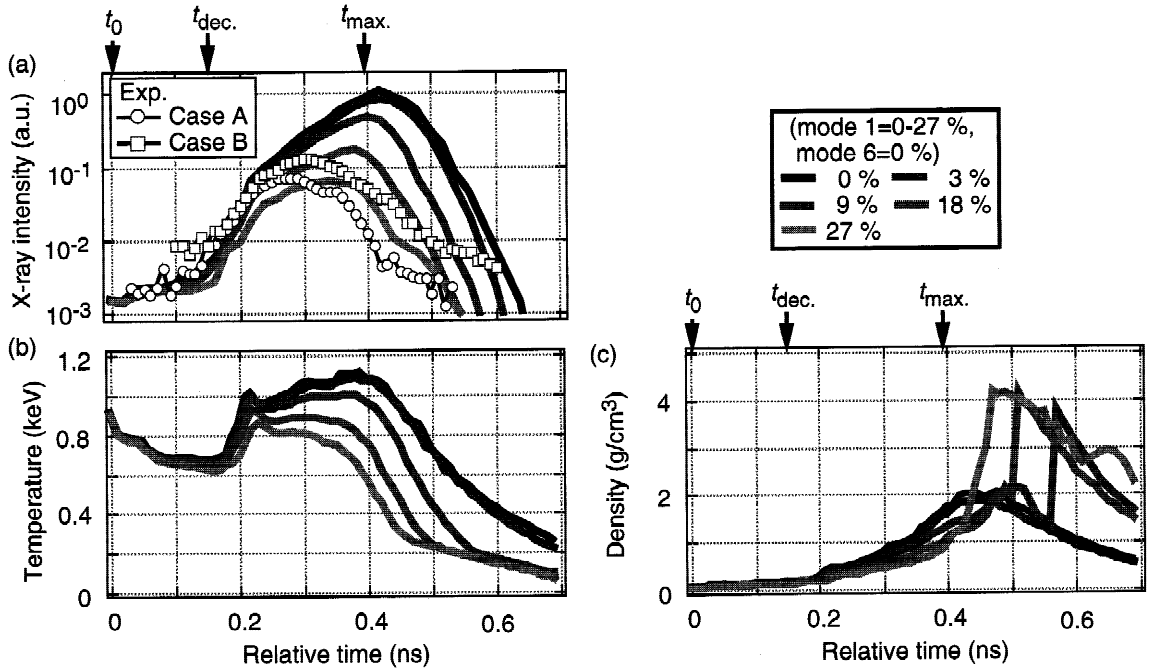

Fig. 14. Temporal histories of the (a) X-ray intensity, (b) temperature, and (c) density of the fuel at the position of the peak temperature on the vertical axis including the center in the 2-D code for calculations with $NU_1 = 0$–27% and $NU_6 = 0$. Experimental results in X-ray intensity at the position of the peak X-ray emission for Cases A and B are also plotted in (a).

https://doi.org/10.1017/S0263034601192177 Published online by Cambridge University Press

does not agree with the experimental results that the bright spot of the X-ray emission remained almost at the same position during the lifetime of the core as shown in Figures 8 and 10.

Figure 14 shows temporal histories of the (a) X-ray intensity, (b) temperature, and (c) density of the fuel at the position of the peak temperature with $NU_1 = 0$–27% and $NU_6 = 0$. The peak temperature decreases rapidly with an increase of NU_1 especially in the late period after $t > 0.2$ ns, while the density increases with an increase of NU_1 in the very late period after $t > 0.4$ ns. This increase of the density appears locally at the bottom of the shell as shown in Figure 13(c) at $t = 0.4$ and 0.5 ns. The experimentally observed X-ray intensities decay rapidly after $t > 0.3$ ns and are far lower than that for a perfectly spherical implosion with $NU_1 = NU_6 = 0$. The 2-D calculations with $NU_1 = 18$ or 27% result in similar features to the experiments, although the decay of the X-ray emission is still faster in experiments than in 2-D calculations after $t > 0.3$ ns.

In 2-D calculations with $\ell = 1$ perturbations, as described above, we found that the fuel can be cooled down by the intrusion of the shell as one spike into the spark and the temporal history of the X-ray intensity at the central position of the core can be explained with $NU_1 = 18$–27% until $t = 0.3$ ns as shown in Figure 14(a). On the other hand, the movement of the bright spot of the X-ray emission in the 2-D calculation does not agree with the experiments. This situation with only NU_1 is not consistent with the experiments, and this indicates that a further cooling mechanism is necessary to explain the experimental results at the late period in the stagnation phase.

Next, we made 2-D calculations taking into account an additional $\ell = 6$ perturbation onto $\ell = 1$. Calculated results are shown in Figures 15 and 16. The velocity perturbations with $\ell = 1$ and $\ell = 6$ were varied in ranges of $NU_1 = 0$–27% and $NU_6 = 0$–20%, respectively. The phase of the $\ell = 6$ perturbation was set so that one of the six positions with the minimum velocity is on the axis of $\ell = 1$. As seen in Figures 15(b) and 15(c), temperature and density distributions with $NU_1 = 18\%$ and $NU_6 = 5\%$ show complicated mixing structures including one large-scale and six small-scale spikes (only three of them are shown in the right half plane) resulting from the coupling of $\ell = 1$ and $\ell = 6$ perturbations. The hot spark mixes with the perturbed shell, and is finally blown away. The cooling of the hot spark takes place with an increase of NU_1 as shown in Figure 16(b). The density increases with $NU_1 = 0$–3% and $NU_6 = 5\%$, which happens locally at the spike's heads of the shell. When a large NU_1

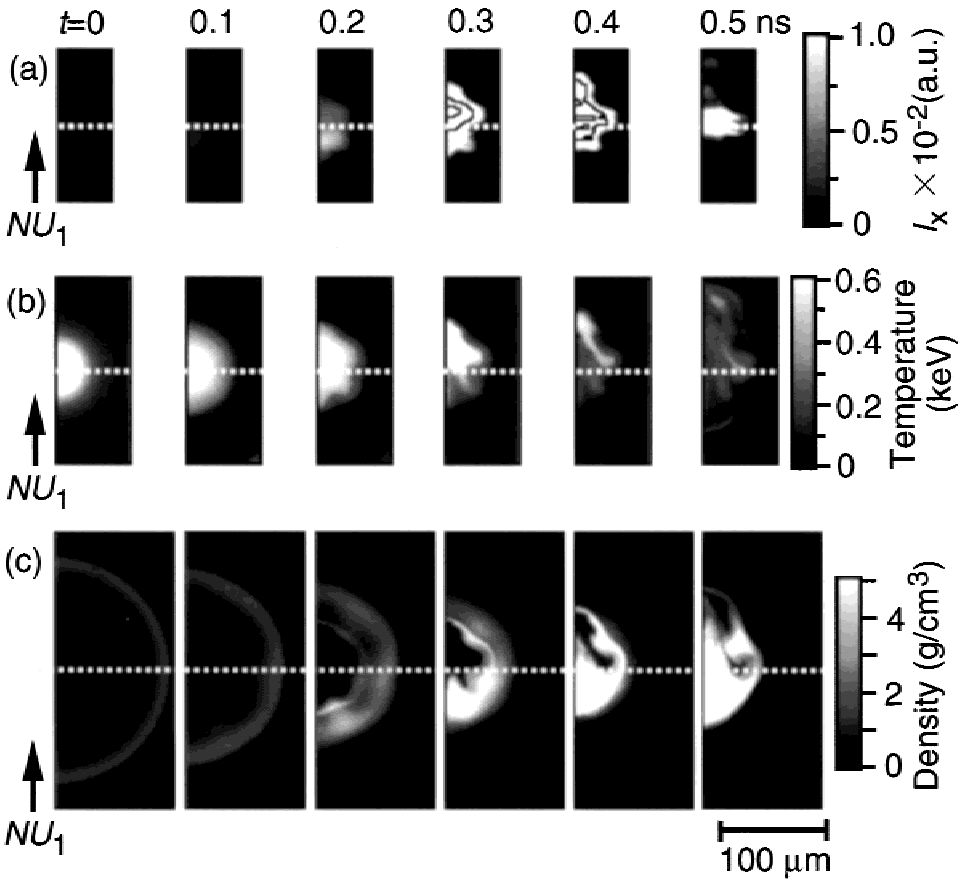

Fig. 15. Calculated snapshots of (a) 2-D X-ray images, and (b) temperature and (c) density distributions with $NU_1 = 18\%$ and $NU_6 = 5\%$. The contour for the 2-D X-ray image is shown at an interval of 0.04 in X-ray intensity (a.u.).

https://doi.org/10.1017/S0263034601192177 Published online by Cambridge University Press

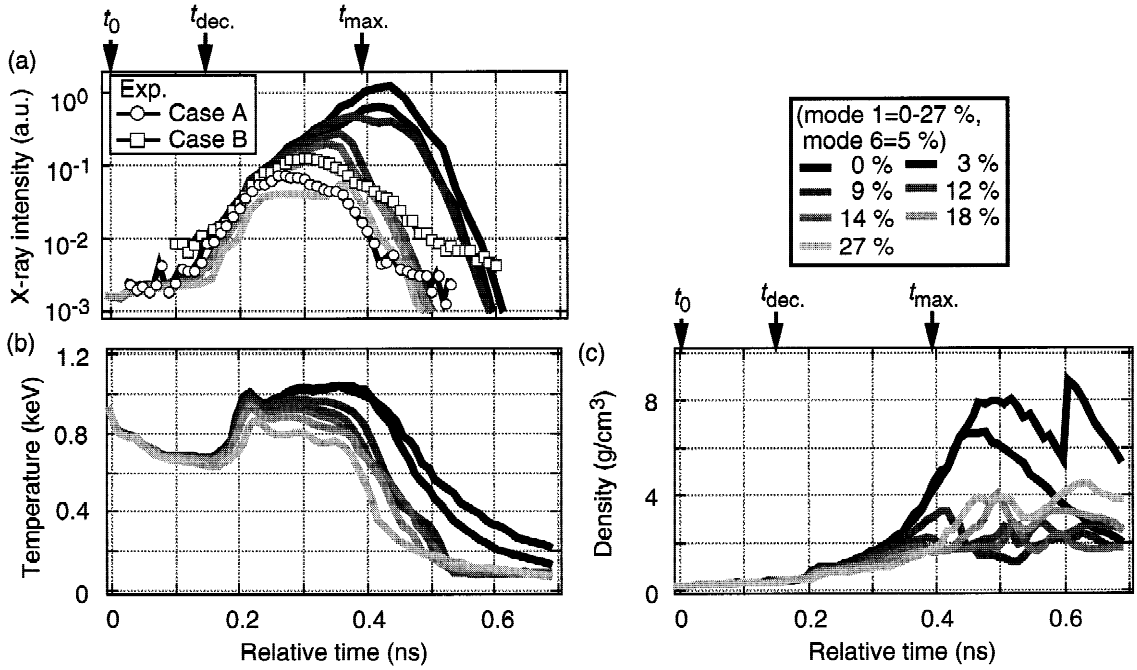

Fig. 16. Temporal histories of the (a) X-ray intensity, (b) temperature, and (c) density of the fuel for various calculations with NU_1 = 0–27% and NU_6 = 0–20% in the same manner shown in Figure 14.

(>9%) is introduced with $NU_6 = 5\%$, the density is almost the same as with the case of NU_1 only ($NU_6 = 0$) shown in Figure 14(c), indicating that the core structure is strongly distorted and the confinement of the fuel is prevented after $t > 0.4$ ns. As shown in Figure 16(a), the calculated X-ray intensities for $NU_1 = 18\%$ with $NU_6 = 5\%$ and $NU_1 = 27\%$ with $NU_6 = 5\%$ are in good agreement with the experiments for Cases B and A, respectively.

Figure 17 shows calculated spatial profiles of the X-ray intensity shown in Figure 15(a) on the vertical axis in the (a) build-up and (b) decaying phase of the X-ray emission. They have asymmetric structures. The decay of the emission is more rapid after $t > 0.4$ ns than in the case with $\ell = 1$ only, and the central position of the emission profile moves only 10 μm or so during the shortened period ($t = 0.24$–0.44 ns), which corresponds to the experimentally observed X ray emission time from the core. This movement of the X-ray profile shown in Figure 17 can be projected to the 2-D viewing plane of the McMIXS in Figure 10, and becomes about 4–8 μm, which is less than the spatial resolution of the McMIXS. This is consistent with the experimental results in Figure 10 that the position of the peak X-ray emission almost did not move. It was found that the coupling of the $\ell = 6$ nonuniformity onto $\ell = 1$ makes the cooling of the

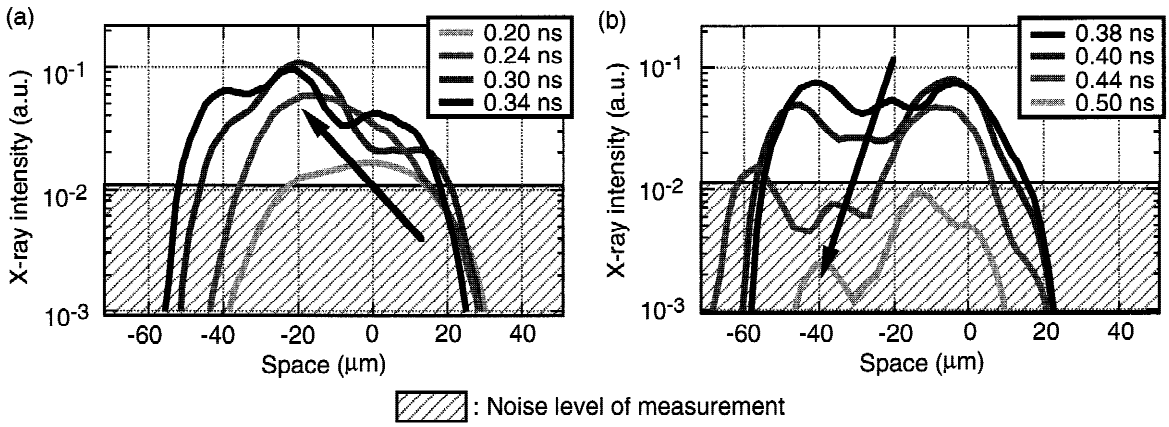

Fig. 17. Calculated spatial profiles of the X-ray intensity shown in Figure 15(a) on the vertical axis in the (a) build-up and (b) decaying phase of the X-ray emission with $NU_1 = 18\%$ and $NU_6 = 5\%$.

https://doi.org/10.1017/S0263034601192177 Published online by Cambridge University Press

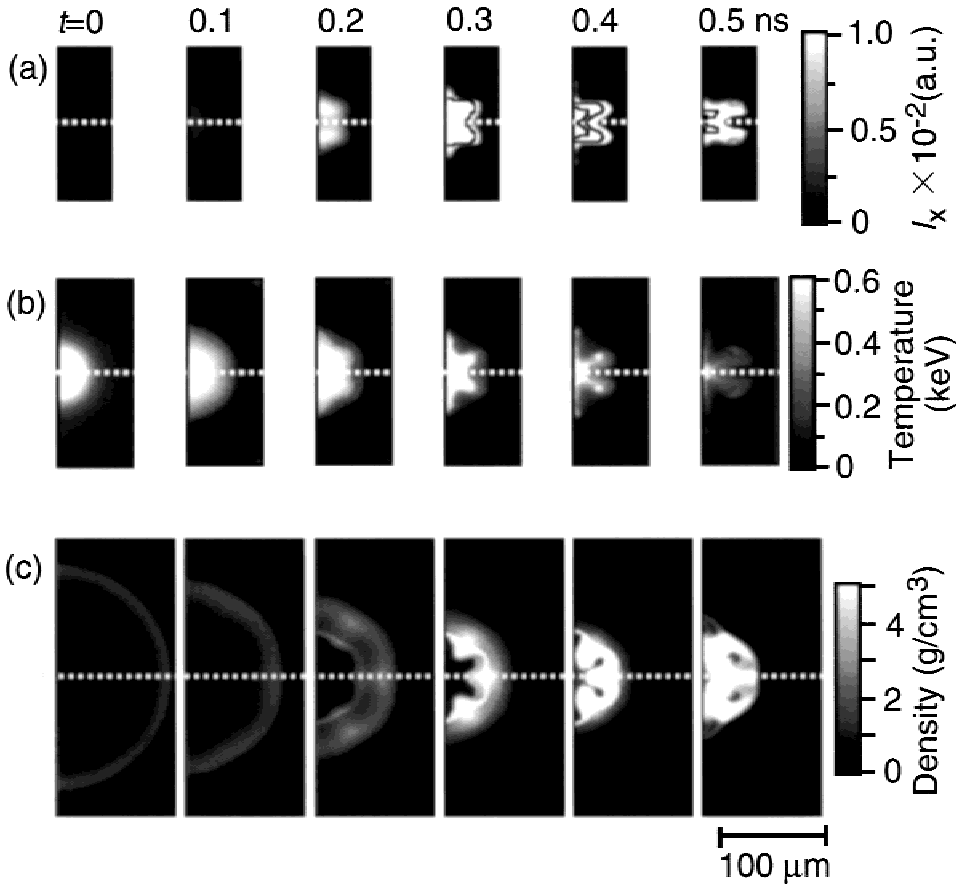

Fig. 18. Calculated snapshots of (a) 2-D X-ray images, and (b) temperature and (c) density distributions with $NU_1 = 0$ and $NU_6 = 5\%$. The contour for the 2-D X-ray image is shown at an interval of 0.25 in X-ray intensity (a.u.).

hot spark faster than with $\ell = 1$ only, and the experimental results in X-ray history are well explained with such nonuniformities of $\ell = 1$ coupled with additional $\ell = 6$.

Finally, we examined effects of the nonuniformity with $\ell = 6$ only. Figure 18 shows results of the 2-D calculation with $NU_1 = 0$ and $NU_6 = 5\%$. The phase for $\ell = 6$ was set so that one of the six positions with the minimum velocity is on the vertical axis. In this case, six spikes (only three of them in the right half are shown) are symmetrically formed and collide at the center of the target. A small fraction of the fuel is confined in the six spike's heads and becomes high temperature. The peak density is at the spike's heads. Figures 19(b) and 19(c) show that the temperature decreases and the density increases with an increase of NU_6. This behavior takes place only in the small fraction confined with spikes at the center of the target.

The position of the bright X-ray emission in the calculated X-ray image remains at the center as shown in Figure 18(a), which is consistent with the experiments in Figures 8 and 10. However, the shape of the X-ray image in Figure 18(a), which has a structure with spikes corresponding to the $\ell = 6$ nonuniformity, does not agree with the experimentally observed X-ray images shown in Figure 10. The X-ray intensity at the central position of the core shown in Figure 19(a) decreases a bit with an increase of NU_6, but the experimentally observed X-ray intensity is far below the 2-D calculation and can not be reproduced even with $NU_6 =$ 20%. Such a situation with only NU_6 is not consistent with the experiments and is unrealistic.

As described above, the experimentally observed X-ray and neutron properties can be reproduced by 2-D simulations with combinations of NU_1 and NU_6. Figure 20 shows the parameter space of NU_1 and NU_6. The light and dark shaded regions are the required conditions for reproducing the experimentally observed X-ray and neutron data for Case A and B implosions, respectively. The most probable parameters are $NU_1 = 18$–22% and $NU_6 = 2$–6% for Case A, and $NU_1 = 13$–17% and $NU_6 = 2$–6% for Case B. NU_1 for Case A is larger than that for Case B, which is consistent with all experimental data, while NU_6 is presumably at the same level for the both cases. An amplitude NU_1' in implosion velocity can be roughly estimated in a different way from a shift Δs of the imploded core from the initial center as $NU_1' = \Delta s / R_0$, if one assumes that an implosion velocity and its nonuniformity are constant in time. Here, R_0 is the initial radius of the target. The experimentally observed shift of the core in Figure 2 gives us $NU_1' = 13.8 \pm 3.0\%$ for Case A and $NU_1' = 5.5 \pm 2.6\%$ for Case B. NU_1' for Case A is larger than

https://doi.org/10.1017/S0263034601192177 Published online by Cambridge University Press

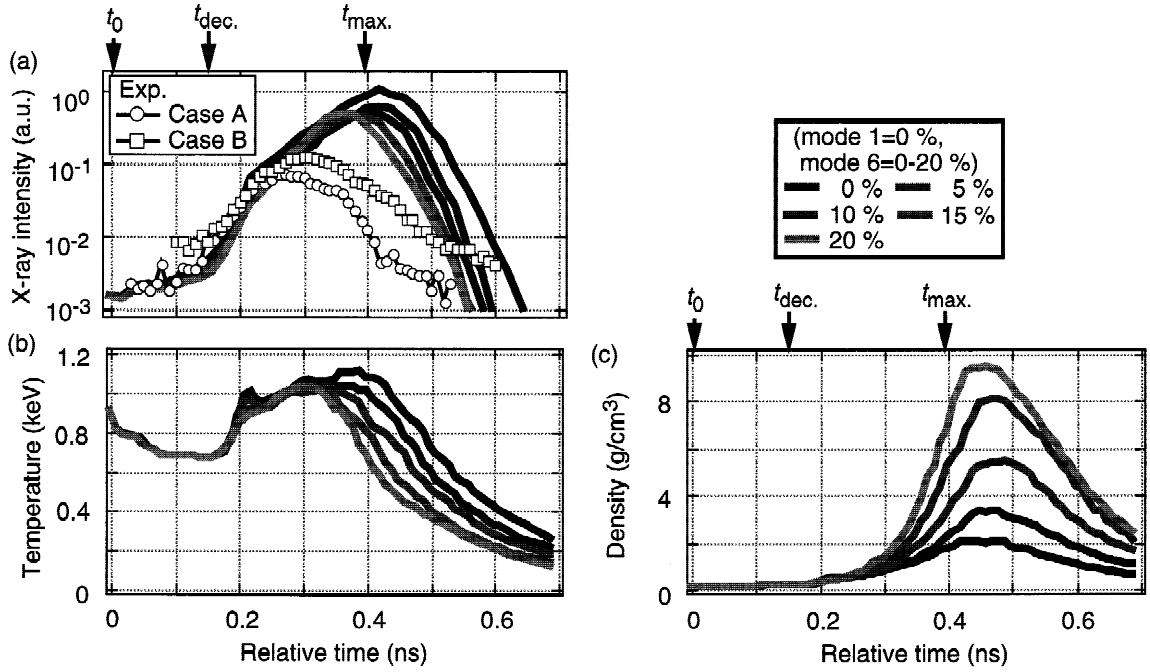

Fig. 19. Temporal histories of the (a) X-ray intensity, (b) temperature, and (c) density of the fuel for various calculations with $NU_1 = 0$ and $NU_6 = 0$–20% in the same manner as shown in Figure 14.

that for Case B, which is consistent with the results obtained in Figure 20 except that the amplitude of NU_1' is smaller by a factor of about two than that of NU_1. This is because we assumed that the implosion nonuniformity at $t = t_0$ in the 2-D calculation is only the velocity perturbation. Of course, such an implosion nonuniformity consists of both the velocity and position perturbations of the shell in a real implosion. Therefore, the values for NU_1 and NU_6 in velocity are obviously overestimation. From these discussions, we conclude that the $\ell = 1$ nonuniformity in implosion velocity is about 14–22% for Case A and about 6–17% for Case B, and the $\ell = 6$ nonuniformity is of the order of 5–10% for the two cases.

An essential feature of the core dynamics observed in this experiment is that the $\ell = 1$ nonuniformity plays an important role on the degradation of the hot-spark formation in the core plasmas, and the existence of the multimode nonuniformity such as $\ell = 6$ coupled to $\ell = 1$ is essential to explain the faster cooling of the core as observed in the experiments.

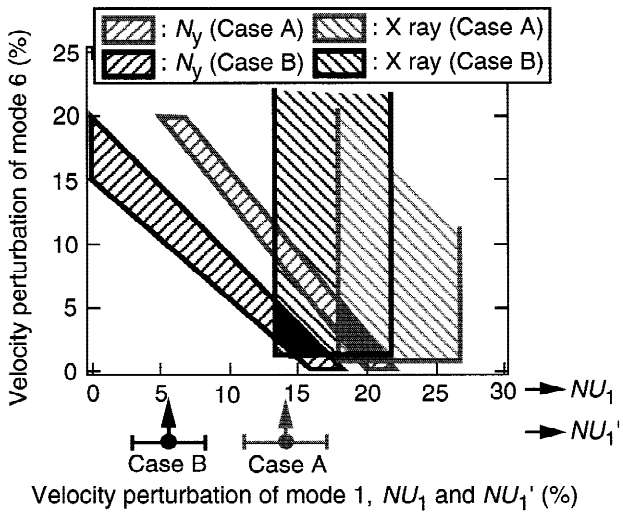

Fig. 20. Summary of comparisons of the experimental and calculated results of X rays and neutrons in the NU_1–NU_6 parameter space. Amplitudes of the velocity nonuniformities derived from the shift of the core of the XPC's data for Cases A and B are also indicated as NU_1'.

4. CONCLUSION

We have performed a series of direct-drive implosion experiments at the Gekko-Xll glass laser with plastic-shell targets filled with fuel gas under relatively low RT growth. The overall implosion dynamics from the acceleration to stagnation phase was observed with a variety of X-ray and neutron diagnostics. It was found that the implosion nonuniformity with $\ell = 1$ due to the drive asymmetry strongly affects the formation process of the hot spark in the imploded core. From comparisons of the experimentally observed properties of X-ray and neutron data in the core plasmas with 1-D and 2-D simulations, it was found that the core plasmas at the late period of the stagnation phase are cooled down not by the $\ell = 1$ nonuniformity only, but as a result of the coupling of the $\ell = 1$ nonuniformity and some other low-modes, for example, $\ell = 6$. A complex spike structure of $\ell = 1$ coupled with some other low-

https://doi.org/10.1017/S0263034601192177 Published online by Cambridge University Press

modes such as $\ell = 6$ was concluded to be essential to explain the observed rapid cooling of the hot spark. The reduced $\ell = 1$ nonuniformity was also found to result in a better core performance. Finally, improvements of the beam power-balance and the beam profiles on the target are essential to reduce implosion nonuniformities. Such efforts are currently underway on the Gekko-XII laser system.

ACKNOWLEDGMENTS

The authors thank O. Maegawa, K. Shimada, A. Fujishima, T. Sonomoto, and M. Oshikawa for their technical support in experiments. We are grateful to Y. Ochi and I. Niki for useful discussions. We also acknowledge technical assistance from our laser, target, diagnostics, and simulation groups. One of the authors (M.H.) acknowledges financial supports from the Japan Society for the Promotion of Science.

REFERENCES

ANDRE, M. *et al.* (1992). *Laser Part. Beams* **10**, 557.
AZECHI, H. *et al.* (1991). *Laser Part. Beams* **9**, 193.
AZECHI, H. *et al.* (1997). *Phys. Plasmas* **4**, 4079.
BAYER, C. *et al.* (1984). *Nucl. Fusion* **24**, 573.
BRADLEY, D.K. *et al.* (1992). *Phys. Rev. Lett.* **68**, 2774.
BRYSK, H. (1973). *Plasma Phys.* **15**, 611.
CABLE, M.D. *et al.* (1994). *Phys. Rev. Lett.* **73**, 2316.
DESSELBERGER, M. *et al.* (1992). *Phys. Rev. Lett.* **68**, 1539.
DITTRICH, T.R. *et al.* (1994). *Phys. Rev. Lett.* **73**, 2324.
HEYA, M. *et al.* (1997). *Rev. Sci. Instrum.* **68**, 820.
HEYA, M. *et al.* (2000). In *Proceedings of International Forum on Advanced High Power Lasers and Applications*, Osaka, Japan. Proceedings of SPIE **3886**, 457.
IZUMI, N. *et al.* (1999). *Rev. Sci. Instrum.* **70**, 1221.
KALANTAR, D.H. *et al.* (1996). *Phys. Rev. Lett.* **76**, 3574.
KATAYAMA, M. *et al.* (1991). *Rev. Sci. Instrum.* **62**, 124.
KATO, Y. *et al.* (1984). *Phys. Rev. Lett.* **53**, 1057.
KATO, Y. *et al.* (1996). In *Proceedings of 12th International Conference on Laser Interaction and Related Plasma Phenomena*, Osaka, Japan, AIP Conference Proceedings **369**, 102 (Woodbury, NY: American Institute of Physics).
KILKENNY, J.D. *et al.* (1988). In *Proceedings of 12th International Conference on Plasma Physics and Controlled Nuclear Fusion Research*, Nice, Paper No IAEA-CN-50/B-I-3 (Vienna: International Atomic Energy Agency).
KOENIG, M. *et al.* (1992). *Laser Part. Beams* **10**, 573.
MARSHALL, F.J. *et al.* (1989). *Phys. Rev. A* **40**, 2547.
MEYER-TER-VEHN, J. (1982). *Nucl. Fusion* **22**, 561.
MIYANAGA, N. *et al.* (1996). In *Proceedings of 1st International Conference on Solid State Lasers for Application to Inertial Confinement Fusion*, Monterey, CA, SPIE **2633**, 183.
NAKANO, H. *et al.* (1993). *Appl. Phys. Lett.* **63**, 580.
NUCKOLLS, J. *et al.* (1972). *Nature (London)* **239**, 139.
RICHARDSON, M.C. *et al.* (1986). *Phys. Rev. Lett.* **56**, 2048.
SHIRAGA, H. *et al.* (1995). *Rev. Sci. Instrum.* **66**, 722.
SHIRAGA, H. *et al.* (1997). *Rev. Sci. Instrum.* **68**, 828.
STROM, E. *et al.* (1990). In *Proceedings of 13th International Conference on Plasma Physics and Controlled Nuclear Fusion Research*, Washington DC, Paper No IAEA-CN-53/B-II-3 (Vienna: International Atomic Energy Agency).
SUNAHARA, A. & TAKABE, H. (1996). *Annual Progress Report*, (Osaka, Japan: Institute of Laser Engineering, Osaka University), p. 232.
TAKABE, H. *et al.* (1988). *Phys. Fluids* **31**, 2884.
TAKABE, H. *et al.* (1989). *Laser Part. Beams* **7**, 175.
TAKAGI, M. & NORIMATSU, T. (1995). *Annual Progress Report* (Osaka, Japan: Institute of Laser Engineering, Osaka University), p. 235.
TSUBAKIMOTO, K. *et al.* (1998). *Jpn. J. Appl. Phys.* **37**, 5560.
YAMANAKA, C. *et al.* (1987). *Nucl. Fusion* **27**, 19.